Volume 13
Number 16
28 April 2025
Pages 7891–8338

Journal of Materials Chemistry C

Materials for optical, magnetic and electronic devices

rsc.li/materials-c

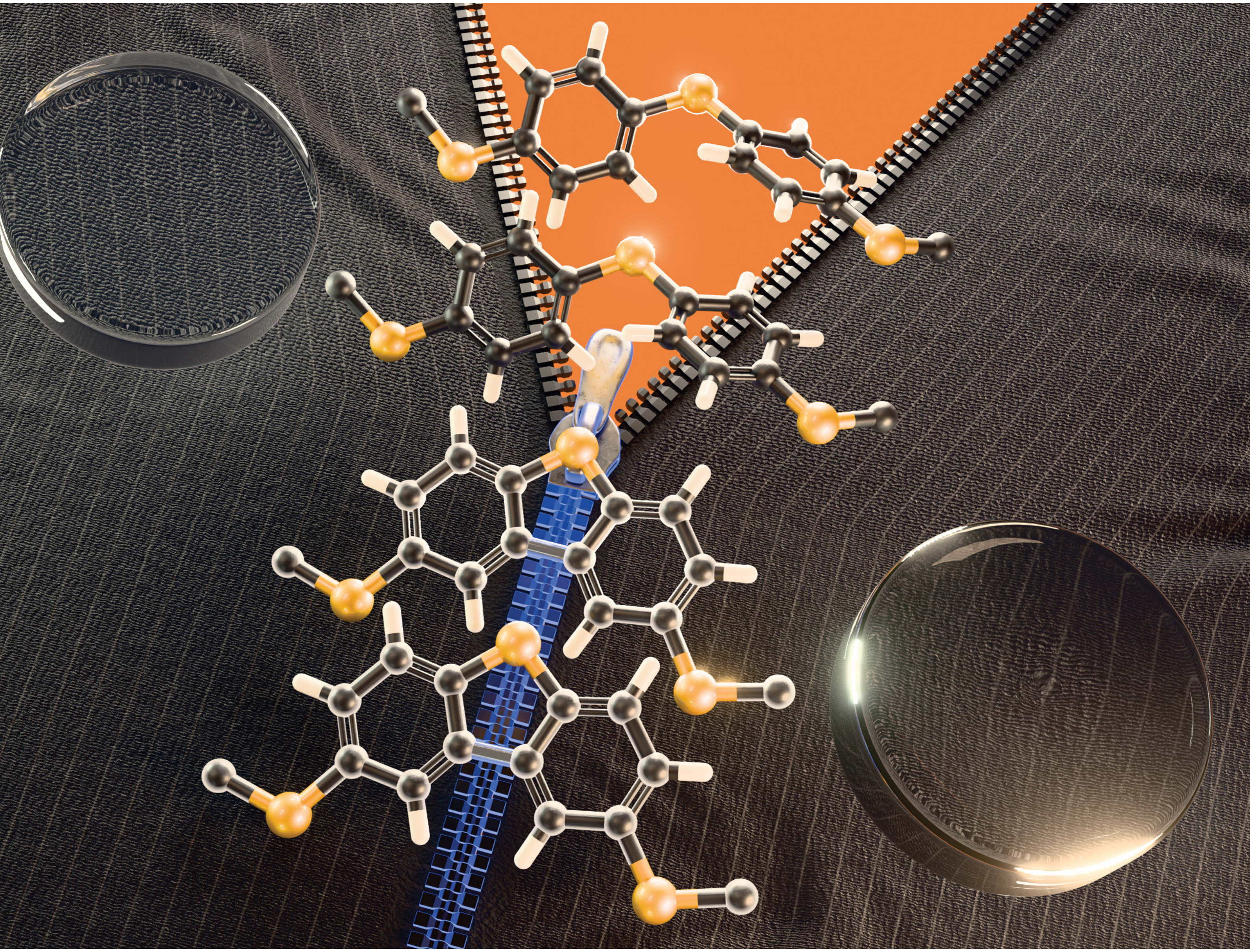

ISSN 2050-7526

ROYAL SOCIETY OF CHEMISTRY

PAPER
Kenichi Oyaizu *et al.*
Poly(dibenzothiophenylene sulfide)s: sulfur-rich annulated frameworks with a wide-range ultrahigh refractive index

Journal of
Materials Chemistry C

ROYAL SOCIETY
OF CHEMISTRY

PAPER

View Article Online
View Journal | View Issue

Check for updates

Cite this: *J. Mater. Chem. C*, 2025, **13**, 7933

Received 26th December 2024,
Accepted 19th March 2025

DOI: 10.1039/d4tc05458j

rsc.li/materials-c

Poly(dibenzothiophenylene sulfide)s: sulfur-rich annulated frameworks with a wide-range ultrahigh refractive index†

Seigo Watanabe,[a] Zexin An,[b] Hiromichi Nishio,[b] Yoshino Tsunekawa[b] and Kenichi Oyaizu *[ab]

Poly(phenylene sulfide) (PPS) derivatives exhibit remarkable high-refractive properties due to their elevated sulfur content. However, their refractive indices (RIs) have typically been limited to $n_D \sim 1.7$–1.8, primarily due to the sterically hindered side chains required for desirable amorphous properties. In this study, we demonstrate the "PPS-annulation" strategy, which involves the partial fused system of PPS, as a rational molecular design to achieve wide-wavelength ultrahigh RI. In short, poly(dibenzothiophene sulfide) (**PDBTS**), an annulated analog of PPS, is precisely synthesized through oxidative polymerization. **PDBTS** demonstrates an ultrahigh RI of $n_D = 1.85$, excellent thermostability ($T_g = 205$ °C), and a completely amorphous nature owing to its aromatic/sulfur-rich and rigid backbone. Furthermore, **PDBTS** is further functionalized through copolymerization with other PPS derivatives (*e.g.*, hydroxy- or methylthio-substituted PPS) to optimize the balance between their ultrahigh RI (n_D over 1.82) and enhanced visible–near-infrared transparency. Overall, the "PPS-annulation" strategy offers a rational design for polymeric materials with enhanced RI, high thermostability, amorphous characteristics, and exceptional optical properties.

Introduction

Lighting devices, typified by organic light-emitting diodes (OLEDs), are crucial for sustainable energy-to-light conversion systems, requiring high light extraction efficiency alongside additional features such as lightweight and flexibility.[1,2] High-refractive-index polymers (HRIPs) are key components in various optical elements, such as OLED encapsulants and waveguides, contributing to reducing optical loss.[3–5] HRIPs typically exhibit refractive indices (RIs) exceeding 1.7 and offer high transparency in the near-ultraviolet (UV), visible, or near-infrared (NIR) spectra, depending on the specific application.[4]

A typical HRIP design follows the Lorentz–Lorenz equation, involving either (1) increasing the molar refraction $[R]$ and/or (2) decreasing the molecular volume V (*i.e.*, the van der Waals volume of a unit or/and free volume) to enhance the RI of a polymer in the bulk state.[3,4,6–9] Chalcogenide atoms, typically sulfur, and aromatic rings are essential for balancing the RI and other desired properties, such as thermostability and processability, in optical materials.[4,10–12] In this context, previous studies have mainly focused on poly(phenylene sulfide) (PPS) as a promising HRIP backbone due to its excellent RI, thermal, and mechanical properties. While intrinsic PPS is semicrystalline, polymers incorporating oligomeric PPS units with various linkers (imide,[13–16] triazine,[17,18] and others[19–21]) or network structures[22–24] provide amorphous HRIPs with high visible or NIR transparency. In contrast, we have demonstrated PPS derivatives[4] (Fig. 1, left) with functional side groups displaying maximum PPS unit density, high solubility, and complete amorphous properties to achieve satisfactory visible transparency and a high RI ($n_D \sim 1.7$–1.8). In particular, hydrogen bonding (H-bonding)[25,26] and sulfur-containing[27] skeletons achieved ultrahigh RI ($n_D = 1.80$–1.85), which was attributed to their maximized density and polarizability.

As another RI enhancement strategy, the annulation (*e.g.*, cyclization) of aromatic rings contributes to reducing molar volume, maximizing polarizability, and promoting amorphous properties due to the rigid skeleton preventing tight π–π interactions. For example, poly(thianthrene sulfide), a sulfide-bridged analog of PPS, exhibits transparency, solution processability, and a significantly high RI ($n_{633} = 1.8020$ at maximum) (Fig. 1, middle).[28] In contrast, poly(dibenzothiophene sulfide) (**PDBTS**) (Fig. 1, right), a direct *o*-phenylene-coupled analog of PPS, could be a better candidate owing to its more compact structure for achieving an even higher RI and enhanced thermostability. While

---

[a] *Research Institute for Science and Engineering, Waseda University, 3-4-1 Okubo, Shinjuku-ku, Tokyo 169-8555, Japan. E-mail: oyaizu@waseda.jp*

[b] *Department of Applied Chemistry, Waseda University, 3-4-1 Okubo, Shinjuku-ku, Tokyo 169-8555, Japan*

† Electronic supplementary information (ESI) available: Monomer synthesis; computational studies; additional NMR and IR spectra of polymers; copolymerization and demethylation studies; and additional thermal/optical properties of the copolymers. See DOI: https://doi.org/10.1039/d4tc05458j

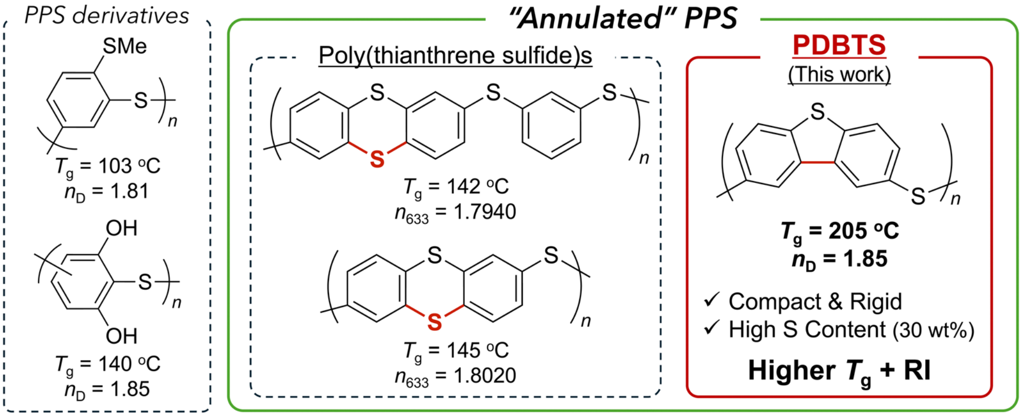

Fig. 1 Ultrahigh-RI and amorphous PPS family: non-annulated PPS derivatives[26,27] (left), poly(thianthrene sulfide)s[28] (middle), and **PDBTS** (this work) (right).

PDBTS has been recognized as an electron-conducting polymer after chemical doping,[29] its optical properties remain unexplored, and in particular, dibenzothiophene (DBT) has seldom been incorporated into previous HRIPs. To our knowledge, the only reported example includes DBT-containing polyimides[30] exhibiting a high RI (n_{633} = 1.7578) and glass transition temperature (T_g = 201 °C). In short, DBT-based HRIPs could potentially achieve elevated RI levels due to their "annulated PPS" backbones with high [R] and compactness.

Herein, we introduce **PDBTS** and its derivatives as a novel ultrahigh-RI PPS family displaying exceptional thermal and optical properties. **PDBTS** is precisely synthesized through the site-selective oxidative polymerization of the DBT-containing disulfide, resulting in an amorphous, thermostable (T_g = 205 °C), and ultrahigh RI (n_D = 1.85) polymer. These outstanding properties stem from its rigid, sulfur-rich, and all-aromatic backbone. Moreover, its optical and thermal properties are further enhanced using the copolymerization approach that combines **PDBTS** with other PPS components to modulate polarizability (specifically sulfur content) and intermolecular H-bond strength. The resulting copolymers exhibited enhanced visible light transparency while maintaining an ultrahigh RI of above 1.8. Overall, the present "annulated PPS" design based on DBT provides a straightforward strategy to enhance the thermal and RI properties of various HRIPs.

Experimental

Materials

All reagents were purchased from Tokyo Chemical Industry Co., Kanto Chemical Co., Junsei Chemical Co., and Kokusan Chemical Co. (for details, refer to the ESI†). Bis(2-methoxyphenyl) disulfide (**OMeDPS**) and bis(2-methylthiophenyl) disulfide (**SMeDPS**) were prepared following our previous reports.[27,31]

Measurements

^{1}H (500 MHz) and ^{13}C (including DEPT) (125 MHz) nuclear magnetic resonance (NMR) spectra were recorded using a JEOL ECX-500 NMR spectrometer. Fast atom bombardment mass (FAB-MS) spectra were obtained using JMS-GCMATE II. Fourier-transform infrared spectra were recorded on a JASCO FT/IR 6100 spectrometer with KBr pellets. Cyclic voltammetry (CV) was performed with a BAS ALS 660D using a three-electrode system, where the working, counter, and reference electrodes were a Pt electrode (φ = 1.6 mm), a Pt wire, and an Ag/AgCl electrode, respectively. In the CV measurement, the potential was measured against an external standard (ferrocene (Fc)/ferrocenium (Fc$^+$) redox couple, $E_{1/2}$ = 0.45 V *vs.* Ag/AgCl). Ultraviolet-visible (UV-vis) spectra were recorded using a JASCO V-670 spectrometer at a scan rate of 100 nm min^{-1}. Size exclusion chromatography (SEC) was performed using a SHIMAZU CBM-20A and SPD-20MA system equipped with a TOSOH TSKgel SuperHM-N column (detectors: UV and RI) and chloroform as the eluent (flow rate: 0.3 mL min^{-1}), and molecular weight was calibrated with polystyrene standards. Powder X-ray diffraction (XRD) profiles were collected with a Rigaku RINT-Ultima III using a Cu target X-ray source (CuKα: 1.54 Å). Thermogravimetric analyses (TGA) were conducted with Rigaku TG8120 under a nitrogen flow from room temperature to 500 °C at a heating rate of 10 °C min^{-1}. Differential scanning calorimetry (DSC) was performed using TA Instruments Q200 in the temperature range of 40–250 °C at a scan rate of 20 °C min^{-1}. The thickness of a polymer film was determined by using a stylus profiler (KLA Tencor P-6).

Optical property measurements

The RI spectra (n, k) were analyzed through spectroscopic ellipsometry in the film state using a Horiba UVISEL ERAGMS iHR320 spectrometer. The Abbe numbers in the visible (ν_D) and NIR (ν_{NIR}) ranges were calculated based on the definitions in eqn (1) and (2):[15]

$$\nu_D = \frac{n_D - 1}{n_F - n_C} \tag{1}$$

$$\nu_{NIR} = \frac{n_{829} - 1}{n_{637} - n_{1306}} \tag{2}$$

where n_F, n_D, n_C, n_{637}, n_{829}, and n_{1306} represent the RIs at the F line (486.1 nm), D line (589.3 nm), C line (656.3 nm), 637 nm, 829 nm, and 1306 nm, respectively. The RI at infinite wavelength

(n_∞) was determined using the simplified Cauchy's formula[4] ($n = n_\infty + D\lambda^{-2}$, where D is a coefficient and λ denotes wavelength) in the wavelength range exceeding 600 nm, well beyond the resonance region (<400 nm) for the UV-vis absorption.

Synthesis of PDBTS

A typical procedure is outlined as follows (entry 3 in Table 1). To a 10 mL flask were added 2,3-dichloro-5,6-dicyano-1,4-benzoquinone (DDQ) (0.23 g, 1.0 mmol) and trifluoroacetic acid (TFA) (25 μL, 0.32 mmol) in 1,2-dichloroethane (DCE) (2 mL). Subsequently, **DBTDPS** (0.43 g, 1.0 mmol) was added to the solution and stirred at room temperature for 20 h. The resulting mixture was diluted by further adding DCE (5 mL) and was then precipitated in methanol with 5 vol% hydrochloric acid (300 mL in total). The precipitate was collected by filtration, was washed successively with methanol, aqueous potassium hydroxide, and water, and was then dried *in vacuo*. The crude product was dissolved in chloroform and was reprecipitated with acetone with 5 vol% hydrochloric acid (300 mL in total). The precipitate was collected through filtration, was successively washed with acetone, potassium hydroxide aqueous, and water, and was then dried *in vacuo* to yield **PDBTS** as a white powder (yield: 0.21 g, 49%).

Synthesis of PDBTS–OMePPS copolymer (CP1)

A typical procedure is outlined as follows (run 2 in Table 2). To a 10 mL flask was added DDQ (0.46 g, 2.0 mmol) with DCE (2 mL) and TFA (50 μL, 0.66 mmol). The monomer mixture, consisting of **DBTDPS** (0.43 g, 1.0 mmol) and **OMeDPS** (0.28 g, 1.0 mmol), was added into the solution and stirred at room temperature for 20 h. After diluting with an additional DCE (6 mL), the solution was precipitated in methanol containing 5 vol% hydrochloric acid (300 mL in total). The resulting precipitate was collected by filtration, was washed successively with methanol, aqueous potassium hydroxide, and water, and was then dried *in vacuo*. The product was reprecipitated with chloroform/acetone with 5 vol% hydrochloric acid. The resulting precipitate was washed with acetone, aqueous potassium hydroxide, and water, and was dried *in vacuo* to obtain **CP1** as a white powder (yield: 0.27 g, 39%).

Synthesis of PDBTS–SMePPS copolymer (CP2)

A typical procedure is outlined as follows (run 5 in Table 2). To a 10 mL flask was added DDQ (0.46 g, 2.0 mmol) with DCE (1 mL) and TFA (50 μL, 0.66 mmol). Once the solution became homogeneous, the monomer mixture (**DBTDPS** (0.43 g, 1.0 mmol) and **SMeDPS** (0.31 g, 1.0 mmol)) dissolved in DCE (1 mL) was added and was stirred at room temperature for 20 h. After diluting with additional DCE (6 mL), the solution was precipitated in methanol with 5 vol% hydrochloric acid (300 mL in total). The resulting precipitate was collected by filtration, was washed successively with methanol, aqueous potassium hydroxide, and water, and was then dried *in vacuo*. The product was reprecipitated using chloroform/acetone with 5 vol% hydrochloric acid. The precipitate was washed with acetone, aqueous potassium hydroxide, and water, and was dried *in vacuo* to obtain **CP2** as a white powder (yield: 0.32 g, 42%).

Synthesis of PDBTS–OHPPS copolymer (CP3)

A typical procedure is outlined as follows (run 8 in Table S1, ESI†). To a 30 mL flask was added **CP1** (0.20 g, 0.22 mmol of –OMe) and was dissolved in dichloromethane (6.12 mL) under an Ar atmosphere. After cooling to 0 °C, a 1 M BBr_3 solution in dichloromethane (3.68 mL, 3.68 mmol) was added under inert conditions. The mixture was stirred at 0 °C for 20 min and then at room temperature for 20 h. The reaction mixture was then quenched with water (6 mL) and the solvent was evaporated using a rotary evaporator. The crude product was dissolved in 6 mL of *N*,*N*-dimethylformamide (DMF) and precipitated in water with 5 vol% hydrochloric acid (200 mL). The resulting precipitate was collected by filtration, was washed with water, and was dried *in vacuo*. The product was redissolved in DMF and was reprecipitated in water containing 5 vol% hydrochloric

Table 1 Oxidative polymerization of **DBTDPS**[a]

Entry	[**DBTDPS**] (M)	Time (h)	Yield (%)	M_n[b] ($\times10^3$)	M_w[b] ($\times10^3$)	M_w/M_n[b] (—)
1	0.5	20	33	0.6	0.7	1.2
2	0.5	40	35	0.9	1.2	1.3
3	1.0	20	49	0.9	1.3	1.4

[a] Temp. = r.t., [DDQ] = [monomer] = 3 eq., [acid] = 1 eq. [b] Determined by SEC (chloroform).

Table 2 Syntheses of **CP1** and **CP2**

Run	Polymer	Yield (%)	Feed ratio of [**DBTDPS**] (—)	Unit ratio x[b] (—)	M_n[c] ($\times10^3$)	M_w[c] ($\times10^3$)	M_w/M_n[c] (—)
—	**PDBTS**[a]	49	1.00	1.00	0.9	1.3	1.4
1	**CP1**	29	0.75	0.65	1.5	1.9	1.3
2	**CP1**	36	0.50	0.46	1.8	2.6	1.5
3	**CP1**	42	0.25	0.25	3.1	3.9	1.3
4	**CP2**	25	0.75	0.75	0.8	1.2	1.5
5	**CP2**	42	0.50	0.48	1.0	1.6	1.6
6	**CP2**	53	0.25	0.24	1.2	1.6	1.3

[a] Entry 3 in Table 1. [b] Determined by ^{1}H NMR. [c] Determined by SEC (chloroform).

acid (20-fold excess). After purifying and drying following a similar protocol, **CP3** was obtained as a white powder (yield: 0.15 g, 75%).

Film preparation for optical measurements

Thin films of the polymers were fabricated *via* drop-casting or spin-coating methods, as described in our previous report.[27]

Samples for UV-vis measurements. A polymer solution in 1,1,2,2-tetrachloroethane (for **PDBTS**, **CP1**, and **CP2**, 10 mg mL^{-1}) or DMF (for **CP3**, 10 mg mL^{-1}) was filtered using a PTFE filter (pore size: 0.2 μm). Subsequently, 400 μL of the filtered solution was deposited onto a glass substrate and dried *in vacuo* at 40 °C (for **PDBTS**, **CP1**, and **CP2**) or 90 °C (for **CP3**) to obtain a transparent thin film.

Samples for spectroscopic ellipsometry. An above-filtrated polymer solution in 1,1,2,2-tetrachloroethane (for **PDBTS**, **CP1**, and **CP2**, 50 mg mL^{-1}) or DMF (**CP3**, 50 mg mL^{-1}) was applied onto a Si wafer. The solution was spin-coated with the following procedure: (1) slope = 3 s for 800 rpm, maintained for 45 s; (2) slope = 3 s for 1500 rpm, maintained for 50 s, followed by (3) a final slope = 3 s. A thin-film-coated sample was dried *in vacuo* at 40 °C (**PDBTS**, **CP1**, and **CP2**) or 100 °C (**CP3**) to obtain a transparent thin film.

Results and discussion

Synthesis of PDBTS

The target **PDBTS** was synthesized by the oxidative polymerization of bis(3-dibenzothiophenyl) disulfide (**DBTDPS**). The **DBTDPS** monomer was prepared through a two-step synthesis: the copper-assisted thiolation of 3-bromodibenzothiophene followed by the thiol oxidation, as reported previously[27,32] (refer to the ESI† for details). **DBTDPS** was characterized using NMR and FAB-MS measurements (Fig. S1–S5, ESI†). The electrochemical properties of **DBTDPS** were verified by CV, revealing an irreversible oxidation peak at 1.73 V *vs.* Ag/$AgNO_3$, a higher potential than that of another typical DPS family[26,27,31] (Fig. S6, ESI†). To elucidate the rationale, the optimized geometries of **DBTDPS** were estimated by the density functional theory (DFT) calculations (Fig. S7, ESI†). The highest occupied molecular orbital (HOMO) of **DBTDPS** was less distributed around the disulfide bonds due to the delocalized π-electrons resulting from the annulated DBT rings, indicating its lower oxidation ability (Fig. S7b, ESI†). The reduced nucleophilicity of **DBTDPS** caused by the annulated structures also lowers its reactivity towards electrophilic substitution reactions, which might lead to lower polymerization degree.

Despite such less reactive nature of **DBTDPS**, its oxidative polymerization proceeded smoothly in a halogenated solvent with a low donor number, specifically DCE, under acidified conditions (Fig. 2a and Table 1). Since the oxidative polymerization of aromatic disulfides proceeds *via* the chain-growth polycondensation mechanism,[33] higher monomer concentration and longer reaction time generally increase molecular weight and polymer yield.[31] Starting from the benchmark condition (entry 1: [monomer] = 0.5 M, time: 20 h), longer reaction time (entry 2: 40 h) or higher monomer concentration (entry 3: 1 M) resulted in higher yield and molecular weight, with the latter optimization giving the most efficient results. Still, the resulting **PDBTS**

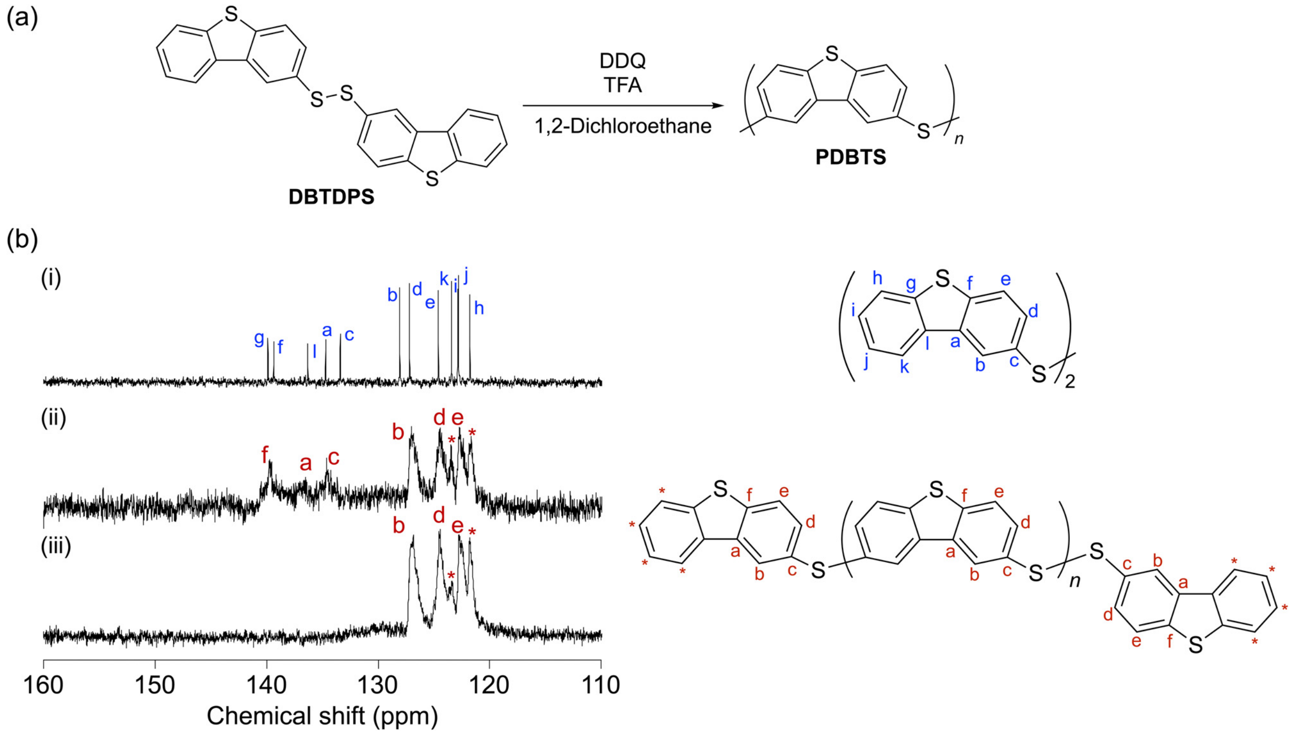

Fig. 2 Oxidative polymerization of **DBTDPS**. (a) Scheme. (b) Expanded ^{13}C NMR spectra of (i) **DBTDPS**, (ii) **PDBTS**, and (iii) **PDBTS** (DEPT135) in chloroform-d (*: terminal aromatic carbons). The overall spectra are depicted in Fig. S4, S9 and S10 (ESI†), respectively.

exhibited an oligomeric molecular weight up to $M_w = 1.3 \times 10^3$ (entry 3) with a low yield (<50%) due to the lower reactivity of the monomer compared to other typical DPS derivatives.[25,27,31] The ^{1}H NMR spectrum of **DBTDPS** exhibited broadened and multimodal aromatic proton signals attributed to strong π–π interchain interactions between the DBT units (Fig. S8, ESI†). In contrast, the ^{13}C NMR spectrum revealed six distinct signals for the main-chain aromatic carbons, three of which corresponded to the C–H carbons also observed in the DEPT spectrum (Fig. 2b). Due to the low molecular weight of **PDBTS**, several terminal aromatic carbons (labeled * in Fig. 2b(ii) and (iii)) were also detected in the chemical shifts similar to the most peripheral carbons in **DBTDPS** (labeled h–k in Fig. 2b(i)). The IR spectrum showed two emerging bands for the out-of-plane vibrations ($\delta_{C\text{-}H}$: 856 and 876 cm^{-1}) for **PDBTS** (Fig. S11, ESI†), indicating the presence of adjacent and isolated aromatic C–H protons. The stretching of the thiophene rings (1410 cm^{-1})[34] further confirmed the successful polymerization without structural defects. Considering the single-substitution pattern of aromatics with a highly symmetrical skeleton and the aforementioned characterization results, the oxidative polymerization of **DBTDPS** selectively produced **PDBTS** with a single 2,8-substituted DBT skeleton.

To gain insight into the reactivity and regioselectivity of this polymerization system, we revisited the electron distribution of **DBTDPS** estimated by the DFT calculations (Fig. S7, ESI,† *vide supra*). The 6- and 8-position carbons of the disulfide exhibit the highest Mulliken charges, indicating enhanced reactivity with active sulfonium electrophiles (Fig. S7a, ESI†). Furthermore, the HOMO is primarily located at the 8-position, while it is delocalized at the 6-position over the adjacent benzothiophene ring. This suggests a preferential reactivity towards yielding a 2,8-substituted **PDBTS** skeleton (Fig. S7b and c, ESI†). The resulting **PDBTS** was in low yield (up to 49%) and low molecular weight ($M_w \sim 1.3 \times 10^3$ (entry 3 in Table 1)) owing to the high oxidation potential of disulfides. This led to increased delocalization of π-electrons upon the polymerization progress, resulting in reduced Friedel–Crafts reactivity with another aromatic counterpart. Enhancing the reactivity could be achieved by incorporating electron-donating groups into **DBTDPS** to lower its oxidation potential, thereby facilitating polymerization rate and increasing the molecular weight.

Thermal and optical properties of PDBTS

The DSC thermogram of **PDBTS** exhibited the highest glass transition temperature (T_g) of 205 °C among all the PPS

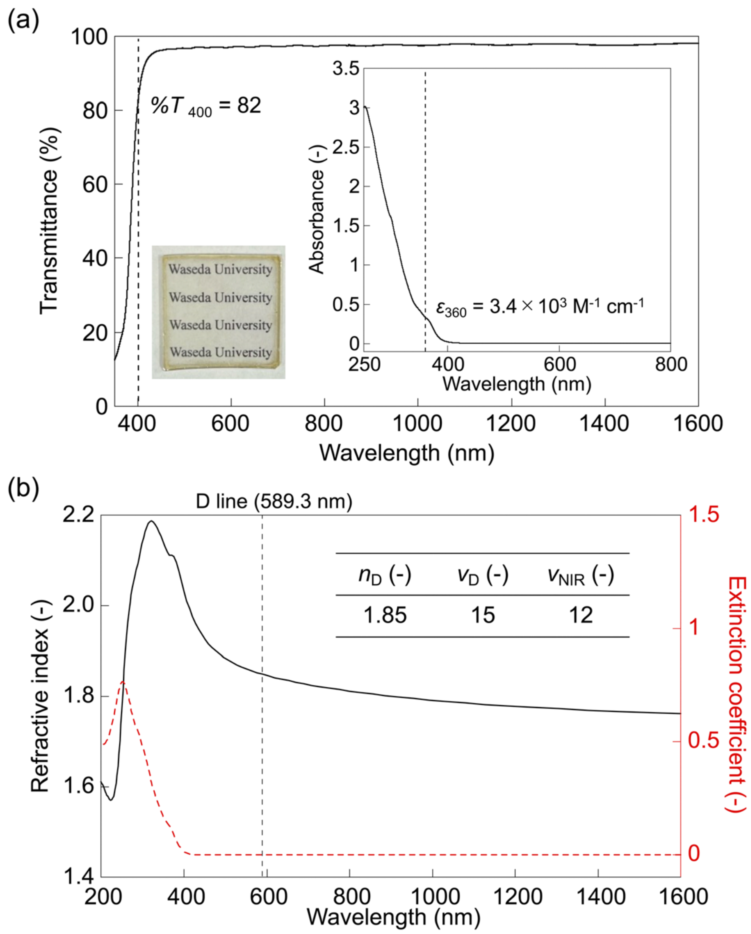

Fig. 3 Optical properties of **PDBTS**. (a) Normalized UV-vis spectrum of the **PDBTS** film with a 1 μm thickness (inset: photograph of the 3.0 μm-thick **PDBTS** film and the UV-vis absorbance spectrum of a 0.1 mM **PDBTS** solution in chloroform). The original spectrum is displayed in Fig. S14 (ESI†). (b) RI spectra of **PDBTS**: *n* (black) and *k* (red) (inset: list of the n_D and Abbe numbers).

families, without any melting behaviors despite the low molecular weight (Fig. S12, ESI†). The presence of the rigid DBT backbone led to a higher rotational barrier compared to the previously studied side-chain[4] or thianthrene-containing[28] PPS derivatives. The XRD profiles also displayed its amorphous nature characterized by a broad halo peak (Fig. S12 inset, ESI†). This was supported presumably due to the bulky aromatic DBT backbone with a bent substitution pattern, resulting in reduced π–π interchain packing compared to the previous phenylene-containing derivatives. This behavior was in line with the findings in the previous **PDBTS** report,[29] where bent 2,8-substitution led to an amorphous phase, while linear-like 3,7-substitution resulted in a semicrystalline phase. Furthermore, the TGA trace revealed a high degradation temperature of T_{d5} = 383 °C (Fig. S13, ESI†), consistent with the excellent thermal stability conferred by the all-aromatic DBT backbone.

Owing to its high solubility, **PDBTS** was fabricated as a thin film through a solution process (see Fig. 3a, inset, left). The drop-cast film exhibited homogeneity and transparency, although it was slightly brownish due to low near-UV transmittance (%T = 82 at 400 nm, for 1 μm thickness) (Fig. 3a). This transparency was comparable to poly(thianthrene sulfide) with a similar backbone (%T = 84 at 400 nm, for 1 μm thickness).[28] Furthermore, **PDBTS** maintained high transmittance from the long-wavelength visible range (>500 nm) to the NIR region (%$T \geqq 97$ above 500 nm) (see Fig. S14, ESI†). At the molecular level, the solution UV-vis spectrum (Fig. 3a, inset, right) of **PDBTS** exhibited a shoulder absorption peak near the visible region (∼360 nm), which was absent in the spectra of non-annulated PPS derivatives.[25,35] This was attributed to the delocalized π-electrons on the annulated DBT rings, inducing the red-shift of the UV-absorption bands. The **PDBTS** solution was also used for spin-coating, and the resulting thin film exhibited an ultrahigh RI (n_D = 1.85) and a moderate Abbe number (ν_D = 15) (Fig. 3b), surpassing the empirical n_D–ν_D trade-off limit.[27] These high-RI characteristics extended to longer wavelengths, with a reasonable NIR Abbe number (ν_{NIR} = 12) and a high infinite-wavelength RI of n_∞ = 1.74 (Fig. S15, ESI†), indicating its potential for NIR optical applications. The extinction coefficient (k) of **PDBTS** (Fig. 3b, red) exhibited a long cutoff resonance wavelength (∼400 nm) resulting in anomalous RI dispersion, which is in line with the shoulder absorption observed in the solution UV-vis spectrum. In conclusion, **PDBTS** demonstrates ultrahigh RIs across a wide wavelength range (visible–NIR region) due to its high sulfur/aromatic content and annulated skeleton, particularly excelling in optical properties in the NIR region comparable to the previous NIR-transparent PIs (n_{633} < 1.8, %T > 90).[15,16,36]

Copolymerization strategy: PDBTS with side-chain-substituted PPS

To balance the superior RI properties of **PDBTS** with sufficient visible transparency, we extended the design concept to **PDBTS**-based copolymers by incorporating another functionalized PPS to enhance the overall optical properties (Fig. 4). To improve visible transparency while maintaining high RI, the counterparts were selected according to the following criteria: side-substituted PPS with polar methoxy groups (**OMePPS: CP1**), polarizable methylthio groups (**SMePPS: CP2**), and H-bondable hydroxy groups (**OHPPS: CP3**). First, **CP1** and **CP2** were prepared through one-step synthesis involving the oxidative polymerization of the corresponding disulfide monomers (Fig. 4a and Fig. S16. ESI†).

Based on the higher solubility and lower oxidation potential of the counterpart DPS monomer,[27,31] the copolymers were

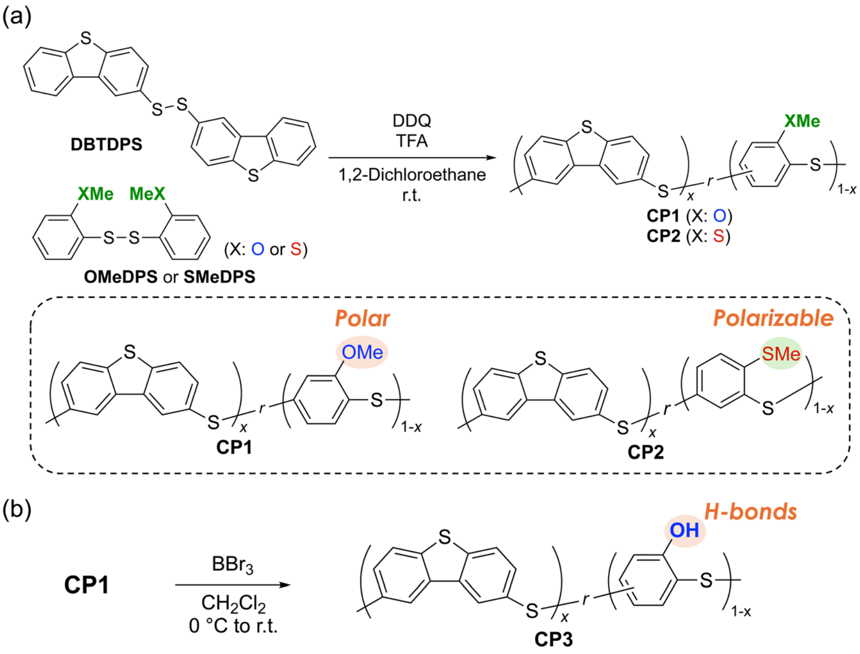

Fig. 4 Synthesis and molecular design of the PPS copolymers containing the **PDBTS** skeleton. (a) Oxidative copolymerization producing the copolymer with either methoxy- (**CP1**) or methylthio-substituted (**CP2**) PPS counterparts. (b) Demethylation of **CP1** to synthesize the H-bondable PPS copolymers (**CP3**).

obtained with a higher yield and improved solubility. Particularly, better results were achieved at a lower **PDBTS** content (x) (Table 2). The molecular weights increased up to $M_w = 3.9 \times 10^3$ and $M_w = 1.6 \times 10^3$ for **CP1** (run 3) and **CP2** (run 6), respectively, indicating that more polar and electron-donating skeletons promote polymerization and enhance solubility. The DOSY-NMR spectra confirmed the presence of copolymers with similar diffusion coefficients for the aromatic and methyl protons (Fig. S17, ESI†). The relative reactivity of each monomer was elucidated by monitoring the time course of copolymerization (Fig. S18–S20, ESI†). Regardless of the counterpart species (**OMeDPS** or **SMeDPS**), the x values were significantly below the feed ratio (x_f) in the initial polymerization stage but gradually approached x_f as the reaction progressed (Fig. S19a and S20a, ESI†). This trend indicated a higher selectivity for DPS with lower oxidation potential, leading to a larger composition, consistent with previous reports on oxidative copolymerization.[27,31] The IR spectra revealed consistent changes in the peak intensity of the stretching bands of the thiophene ring (1400 cm^{-1}) and C–X (X: S or O) bonds ($\nu_{C\text{–}O}$: 1240 cm^{-1}, $\nu_{C\text{–}S}$: 1100 cm^{-1}) in accordance with the overall composition (Fig. S21, ESI†).

The XRD profiles of **CP1** and **CP2** reflect their amorphous features with no specific diffraction of the crystalline phase, following a similar trend to that of the homopolymers (Fig. 5a). Their randomized sequence upon copolymerization also contributes to disordered microstructures with less interchain packing. The TGA and DSC results demonstrated that the copolymers exhibited lower T_{d5} and T_g values at smaller x (Fig. S22, ESI† and Fig. 5b). The DSC thermograms also displayed the thermal behavior of amorphous nature, with a single glass transition for all the copolymers. Furthermore, a series of **CP1** with compact methoxy side chains achieved a higher T_g (above 147 °C) than the side-chain-flexible **CP2** (T_g above 120 °C) while showing superior thermostability to typical side-chain-substituted PPS derivatives,[27] based on the high rigidity of the **PDBTS** backbones.

Owing to the enhanced solubility of the copolymers, **CP1** and **CP2** were solution-processable to fabricate homogeneous thin films (Fig. S23, ESI†). These copolymers exhibited higher visible transparency compared to **PDBTS** (Fig. 5c and Table 3), and particularly **CP1** resulted in better transmittance (over 90%T for 1-μm thick films) attributed to the less-polarizable methoxy groups. The solution UV-vis spectra followed the same trend, suggesting the absence of specific aggregation or charge transfer in the film states (Fig. S24, ESI†). The RI varied systematically depending on the unit ratio, with **CP2** maintaining an ultrahigh RI (n_D = 1.83–1.82) across all compositions, while **CP1** exhibited a lower RI of n_D = 1.80–1.76 (Fig. 5d and Table 3). These differences were primarily attributed to the unit polarizability, resulting in high RIs and low transparency for copolymers with high-[R] skeletons. Considered together with the UV-vis spectra (Fig. 5c: *vide supra*), the RI and transparency of **CP1** and **CP2** changed within the empirical RI-transparency trade-off relationship,[3] without exceeding the overall optical properties of the corresponding homopolymers. In summary, the amount of polarizable units emerged as the key determinant of the optical properties of **CP1** and **CP2**, aligning with the case of a previous **OMePPS**–**SMePPS** copolymer system.[27]

PDBTS copolymers with H-bonding units

Breaking through the latent trade-off boundaries among various HRIP properties (*e.g.*, dual tuning of thermostability, RI, and transparency), we expanded the target copolymer to **CP3**, which incorporates highly polarizable **PDBTS** and H-bondable **OHPPS** units (Fig. 4b and Table S1, ESI†). **CP3** was synthesized

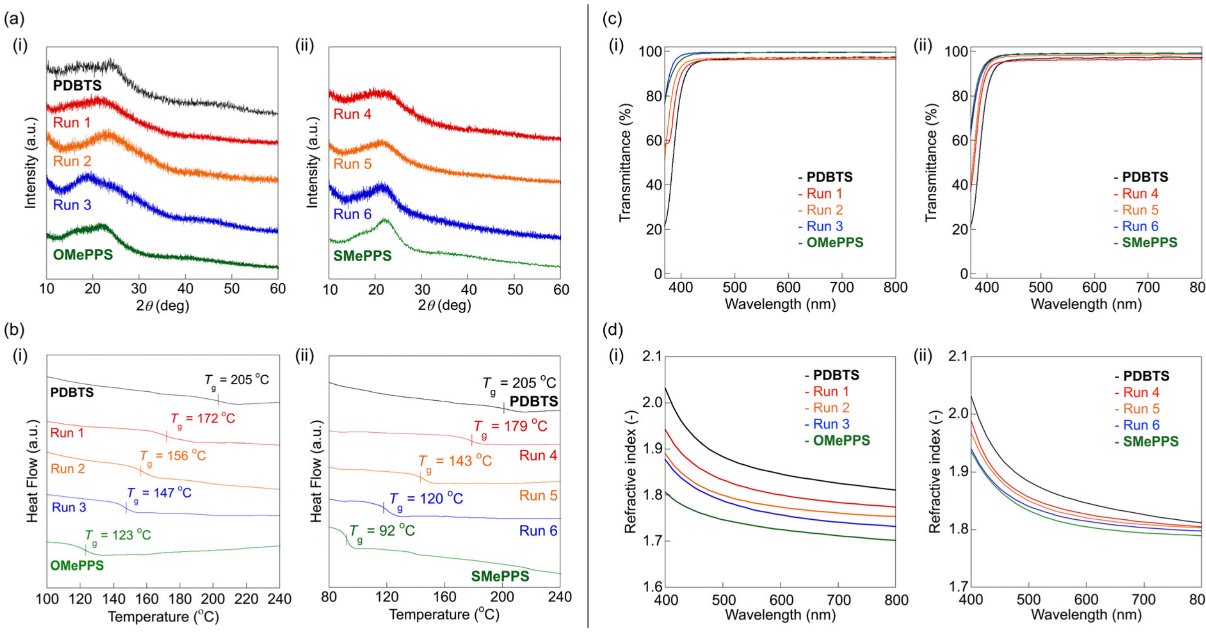

Fig. 5 Thermal and optical properties of (i) **CP1** and (ii) **CP2**: (a) XRD profiles, (b) DSC thermograms (scanning rate: 20 °C min^{-1}, second heating), (c) normalized UV-vis spectra including their corresponding homopolymers (thickness: 1 μm), and (d) RI. Data for the optical properties of **OMePPS** and **SMePPS** were adopted from our previous report (ref. 31 (Copyright © 2020 The Chemical Society of Japan) and ref. 27 (Adopted under the CC-BY-NC-ND 4.0 license), respectively).

Table 3 Optical properties of **CP1** and **CP2**

Run	Polymer	Unit ratio x^b (—)	$\varepsilon^{c,d}$ (10^3 M^{-1} cm^{-1}) at 360 nm	%$T^{c,e}$ at 400 nm	$n_D{}^f$ (—)	$\nu_D{}^f$ (—)
—	**PDBTS**[a]	1.00	3.4	82	1.85	15
1	**CP1**	0.65	2.0	90	1.80	16
2	**CP1**	0.46	1.9	93	1.78	18
3	**CP1**	0.25	1.6	97	1.76	16
—	**OMePPS**	0.00	0.6[g,h]	96[g]	1.73[g]	22[g]
4	**CP2**	0.75	3.3	87	1.83	18
5	**CP2**	0.48	2.7	93	1.82	19
6	**CP2**	0.24	2.5	94	1.82	20
—	**SMePPS**	0.00	1.1[i]	94[i]	1.81[i]	19[i]

[a] Entry 3 in Table 1. [b] Determined by ^{1}H NMR. [c] Determined by UV-vis spectroscopy. [d] Values for chloroform solution (measured concentration: 0.1 mM). [e] Normalized values with 1 μm thickness. [f] Determined by spectroscopic ellipsometry. [g] Data from ref. 31. [h] Determined from the original spectrum data in ref. 31. [i] Data from ref. 27.

by demethylating the methoxy groups of **CP1** using BBr_3,[25,26] leading to complete hydroxylation without any residual methoxy groups, as verified by the ^{1}H NMR spectra (Fig. S25, ESI†). The IR spectra further confirmed the reaction progress, showing H-bonded O–H stretching (ν_{O-H}: 3400 cm^{-1}) and reduced C–O stretching bands (ν_{C-O}: 1240 cm^{-1}) (Fig. S26, ESI†).

In contrast to the strong H-bond interactions, **CP3** was amorphous, showing only broad halos in its XRD profile (Fig. S27, ESI†). This was attributed to the randomly distributed rigid **PDBTS** segments in the **OHPPS**-rich unit sequence, which effectively hindered ordered assembly. From the DSC thermograms, T_g of each **CP3** was slightly lowered through the demethylation of the corresponding **CP2** (Fig. S28, ESI†). Owing to the high rigidity of the **PDBTS** units, the reduced rotational barrier upon demethylation would have a more significant effect than that of intermolecular H-bonds,[25,26] resulting in the lower T_g of **CP3**. The TGA traces displayed the decrease in the 5% degradation temperature (T_{d5}) upon demethylation caused by the presence of reactive hydroxy groups, resulting in earlier pyrolysis (Fig. S29, ESI†).

While intermolecular H-bonds contribute less to the thermal properties, they enhance the optical properties due to their free volume reduction effect without affecting near-UV and visible absorption.[25,26] Fig. 6a and Table S2 (ESI†) summarize the key optical properties of **CP3**. The UV-vis spectra showed similar film transparencies before and after demethylation (%T = 90–97 for **CP1**, 93–96 for **CP3**), with lower absorption in the solution spectra for **CP3** than the corresponding **CP1** (Fig. 6b and Fig. S30, S31(ii), ESI†). Spectroscopic ellipsometry revealed a smaller RI of **CP3** for higher-x compositions (n_D = 1.79, run 7 and n_D = 1.77, run 8) owing to their low-[R] unit contributions. However, an anomalously higher RI was observed for the small-x composition (n_D = 1.82, run 9), surpassing that of **OHPPS** (Fig. 6c).

To investigate this unique behavior, we excerpted the optical properties of runs 3 and 9 as depicted in Fig. 6d. The low-x **CP1** and **CP3** exhibited a simultaneous increase in the RI and transparency upon demethylation, unlike the medium-to-large-x copolymers (run 1/run 7 or run 2/run 8) with similar RI values (Fig. S31 and S32, ESI†). This exceptional trend was attributed to the enhanced intermolecular interactions in the low-x (**OHPPS**-rich) **CP3**, resulting in a reduction of the free volume *via* H-bonding without compromising transparency. In short, the synergistic combination of polarizable **PDBTS** units and **OHPPS** resulted in higher overall [R]/V than the **OHPPS** homopolymer, enabling **CP3** (run 9) to maintain similar transparency while enhancing RI properties. This observation aligns with our previous report on the **OHPPS–SMePPS** copolymer system,[27] supporting the importance of good balance between the highly polarizable groups and H-bonding groups to maximize RIs and transparency simultaneously. In summary, the excessive polarizability of **PDBTS** can be mitigated by co-polymerizing with other PPS derivatives, particularly those with sulfur-containing or H-bonding backbones. This strategy significantly enhances transparency while preserving exceptionally high RIs suitable for visible light applications. Towards even better-balanced RIs and transparency, **PDBTS**-based copolymers with even denser H-bonds (*e.g.* dihydroxy-substituted PPS)[26] and **PDBTS–SMePPS–OHPPS** terpolymers would be the promising targets to improve chain packing while preserving the moderately high polarizability.

Conclusions

In this study, we propose **PDBTS** as a family of ultrahigh-RI polymers. They are characterized by their ''PPS-annulation'' design, which achieves amorphous properties, high polarizability, and good transparency in the broad visible–NIR range. Initially, the **PDBTS** homopolymer exhibited an ultrahigh RI (n_D = 1.85) and excellent thermal properties (T_g = 205 °C) compared to the prior-art PPS derivatives. However, its visible transparency was limited (over 82%T for a 1 μm-thick film) due to an excessive amount of polarizable and annulated skeletons. Therefore, a copolymerization approach with other high-[R] or H-bonding PPS counterparts achieved a better balance of optical properties. In particular, the copolymer **CP2** incorporating **SMePPS** leading to enhanced visible–NIR transparency (over 87%T) while maintaining an ultrahigh RI (n_D over 1.82). Furthermore, the copolymer **CP3** bearing **OHPPS** units displayed an exceptional RI trend with increasing hydroxy content, finally reached a reasonable T_g (143 °C), ultrahigh RI (n_D = 1.82), and higher visible transparency (over 96%T). This trend was attributed to the maximized [R]/V effect through the synergistic contribution of **PDBTS** and H-bonding **OHPPS** units. While **PDBTS**-based polymers are difficult to handle in free-standing states due to their low molecular weight and high

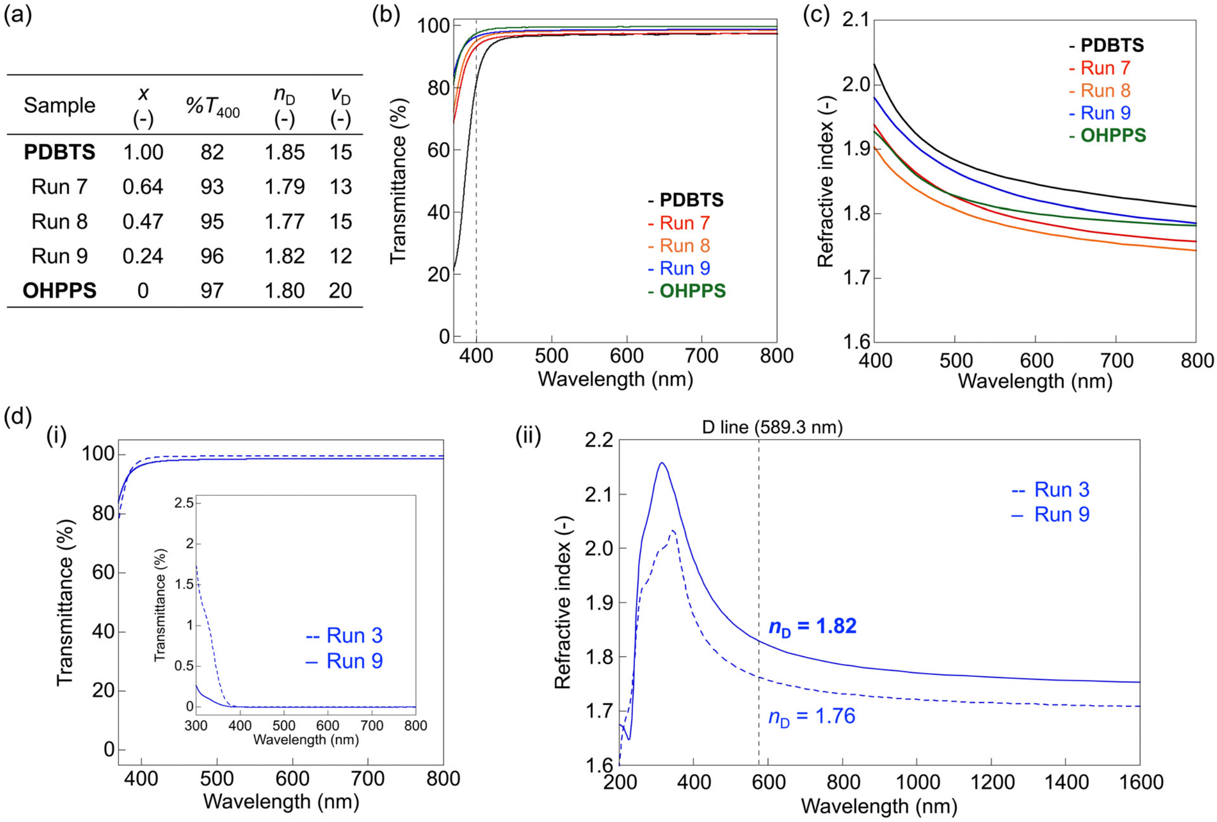

Sample	x (-)	%T_{400}	n_D (-)	ν_D (-)
PDBTS	1.00	82	1.85	15
Run 7	0.64	93	1.79	13
Run 8	0.47	95	1.77	15
Run 9	0.24	96	1.82	12
OHPPS	0	97	1.80	20

Fig. 6 Optical properties of the demethylated copolymer (**CP3**). Data for **OHPPS** were adopted from ref. 25 (Copyright © 2022 American Chemical Society): (a) figures-of-merit, (b) normalized UV-vis spectra of **CP3** and the corresponding homopolymers (thickness: 1 μm). (c) RI of **CP3** and the corresponding homopolymers. (d) Extracted optical properties before and after demethylation from **CP1** (run 3, x = 0.25, dotted line) to **CP3** (run 9, x = 0.24, solid line): (i) normalized film UV-vis spectra (thickness: 1 μm) of the films (inset: UV-vis spectrum of a 0.1 mM solution in DMF). (ii) RI in the near-UV-visible-NIR range.

brittleness, their film-formability and well-balanced thermal/optical properties enable the thin-layer/coating applications in various lighting devices, such as OLEDs,[37,38] light-emitting electrochemical cells (LECs),[39] and waveguides[5,40] toward a higher device efficiency, which will be our continuous research. These results highlight the potential of DBT backbones as an HRIP framework for enhancing thermal and optical properties beyond the empirical limit, allowing their precise tuning from the visible to NIR regions by combining DBT with versatile structural components.

Author contributions

S. W. and K. O. conceived the project and designed the experiments. Z. A. performed most of the experiments with the assistance of S. W., H. N., and Y. T. S. W. conducted the computational calculations. S. W. and K. O. prepared the manuscript. K. O. supervised the project. All authors analyzed the data, discussed the results, and approved the final version of the manuscript.

Data availability

The data supporting this article have been included as part of the ESI.†

Conflicts of interest

The authors declare no conflict of interest.

Acknowledgements

This work was partially supported by Grants-in-Aid for Scientific Research (No. 21H04695 and 22K18335) from MEXT, Japan. S. W. acknowledges Grants-in-Aid from the Satomi Scholarship Foundation and the Nanotechnology Forum Award (Research Organization for Nano and Life Innovation, Waseda University).

Notes and references

1 X. Huang, Y. Qu, D. Fan, J. Kim and S. R. Forrest, *Org. Electron.*, 2019, **69**, 297–300.
2 Y.-F. Liu, J. Feng, Y.-G. Bi, D. Yin and H.-B. Sun, *Adv. Mater. Technol.*, 2019, **4**, 1800371.
3 T. Higashihara and M. Ueda, *Macromolecules*, 2015, **48**, 1915–1929.
4 S. Watanabe and K. Oyaizu, *Bull. Chem. Soc. Jpn.*, 2023, **96**, 1108–1128.
5 A. Nishant, K.-J. Kim, S. A. Showghi, R. Himmelhuber, T. S. Kleine, T. Lee, J. Pyun and R. A. Norwood, *Adv. Opt. Mater.*, 2022, **10**, 2200176.

6 T. S. Kleine, R. S. Glass, D. L. Lichtenberger, M. E. Mackay, K. Char, R. A. Norwood and J. Pyun, *ACS Macro Lett.*, 2020, **9**, 245–259.

7 D. H. Kim, W. Jang, K. Choi, J. S. Choi, J. Pyun, J. Lim, K. Char and S. G. Im, *Sci. Adv.*, 2020, **6**, eabb5320.

8 Y. Zhou, Z. Zhu, K. Zhang and B. Yang, *Macromol. Rapid Commun.*, 2023, **44**, e2300411.

9 S. Wang, X. Li and Y. Tu, *Mater. Horiz.*, 2025, **12**, 15–19.

10 J. J. Griebel, S. Namnabat, E. T. Kim, R. Himmelhuber, D. H. Moronta, W. J. Chung, A. G. Simmonds, K.-J. Kim, J. van der Laan, N. A. Nguyen, E. L. Dereniak, M. E. Mackay, K. Char, R. S. Glass, R. A. Norwood and J. Pyun, *Adv. Mater.*, 2014, **26**, 3014–3018.

11 L. E. Anderson, T. S. Kleine, Y. Zhang, D. D. Phan, S. Namnabat, E. A. LaVilla, K. M. Konopka, L. Ruiz Diaz, M. S. Manchester, J. Schwiegerling, R. S. Glass, M. E. Mackay, K. Char, R. A. Norwood and J. Pyun, *ACS Macro Lett.*, 2017, **6**, 500–504.

12 J. Pyun and R. A. Norwood, *Prog. Polym. Sci.*, 2024, **156**, 101865.

13 N.-H. You, T. Higashihara, S. Ando and M. Ueda, *J. Polym. Sci., Part A:Polym. Chem.*, 2010, **48**, 656–662.

14 Y. Guan, W. Dong, C. Wang and D. Shang, *Polym. Int.*, 2017, **66**, 1044–1054.

15 H. Kim, B.-C. Ku, M. Goh, H. C. Ko, S. Ando and N.-H. You, *Macromolecules*, 2019, **52**, 827–834.

16 S. Xue, X. Lei, Y. Xiao, Y. Liu, Y. Zhang and Q. Zhang, *ACS Appl. Polym. Mater.*, 2024, **6**, 2315–2326.

17 N.-H. You, T. Higashihara, Y. Oishi, S. Ando and M. Ueda, *Macromolecules*, 2010, **43**, 4613–4615.

18 M.-C. Fu, M. Ueda, S. Ando and T. Higashihara, *ACS Omega*, 2020, **5**, 5134–5141.

19 K. Nakabayashi, T. Imai, M.-C. Fu, S. Ando, T. Higashihara and M. Ueda, *Macromolecules*, 2016, **49**, 5849–5856.

20 R. Hifumi and I. Tomita, *Polym. J.*, 2018, **50**, 467–471.

21 S. Watanabe, T. Yano, Z. An and K. Oyaizu, *ChemSusChem*, 2025, **18**, e202401609.

22 L. Fang, J. Sun, X. Chen, Y. Tao, J. Zhou, C. Wang and Q. Fang, *Macromolecules*, 2020, **53**, 125–131.

23 L. Fang, C. Wang, M. Dai, G. Huang, J. Sun and Q. Fang, *Mater. Chem. Front.*, 2021, **5**, 5826–5832.

24 Z. Dou, J. Sun and Q. Fang, *Biomacromolecules*, 2024, **25**, 6155–6163.

25 S. Watanabe and K. Oyaizu, *Macromolecules*, 2022, **55**, 2252–2259.

26 S. Watanabe, H. Nishio, T. Takayama and K. Oyaizu, *ACS Appl. Polym. Mater.*, 2023, **5**, 2307–2311.

27 S. Watanabe, T. Takayama and K. Oyaizu, *ACS Polym. Au*, 2022, **2**, 458–466.

28 Y. Suzuki, K. Murakami, S. Ando, T. Higashihara and M. Ueda, *J. Mater. Chem.*, 2011, **21**, 15727–15731.

29 R. L. Elsenbaumer and L. W. Shacklette, *J. Polym. Sci., Polym. Phys. Ed.*, 1982, **20**, 1781–1787.

30 J.-G. Liu, Y. Nakamura, C. A. Terraza, Y. Shibasaki, S. Ando and M. Ueda, *Macromol. Chem. Phys.*, 2008, **209**, 195–203.

31 S. Watanabe and K. Oyaizu, *Bull. Chem. Soc. Jpn.*, 2020, **93**, 1287–1292.

32 Y. Liu, J. Kim, H. Seo, S. Park and J. Chae, *Adv. Synth. Catal.*, 2015, **357**, 2205–2212.

33 F. Aida, Y. Takatori, D. Kiyokawa, K. Nagamatsu, H. Nishide and K. Oyaizu, *Chem. Lett.*, 2015, **44**, 767–769.

34 C. L. Garcia and J. A. Lercher, *J. Phys. Chem.*, 1992, **96**, 2669–2675.

35 S. Watanabe, Y. Tsunekawa, T. Takayama and K. Oyaizu, *Macromolecules*, 2024, **57**, 2897–2904.

36 K.-H. Nam, A. Lee, S.-K. Lee, K. Hur and H. Han, *J. Mater. Chem. C*, 2019, **7**, 10574–10580.

37 Q. Wei, R. Pötzsch, X. Liu, H. Komber, A. Kiriy, B. Voit, P.-A. Will, S. Lenk and S. Reineke, *Adv. Funct. Mater.*, 2016, **26**, 2545–2553.

38 D. W. Kim, J. W. Han, K. T. Lim and Y. H. Kim, *ACS Appl. Mater. Interfaces*, 2018, **10**, 985–991.

39 S. Watanabe, L. M. Cavinato, V. Calvi, R. van Rijn, R. D. Costa and K. Oyaizu, *Adv. Funct. Mater.*, 2024, **34**, 2404433.

40 J. Zhang, T. Bai, W. Liu, M. Li, Q. Zang, C. Ye, J. Z. Sun, Y. Shi, J. Ling, A. Qin and B. Z. Tang, *Nat. Commun.*, 2023, **14**, 3524.